

RESEARCH ARTICLE

Biomolecular Engineering, Bioengineering, Biochemicals, Biofuels, and Food

Numerical study of biomass gasification combined with CO₂ absorption in a bubbling fluidized bed

Dali Kong¹ | Shuai Wang¹  | Kun Luo^{1,2}  | Jianren Fan^{1,2}

¹State Key Laboratory of Clean Energy Utilization, Zhejiang University, Hangzhou 310027, China

²Shanghai Institute for Advanced Study, Zhejiang University, Shanghai 200120, China

Correspondence

Shuai Wang and Kun Luo, State Key Laboratory of Clean Energy Utilization, Zhejiang University, Hangzhou 310027, China. Email: wshuai2014@zju.edu.cn and zjulk@zju.edu.cn

Funding information

Fundamental Research Funds for the Central Universities, Grant/Award Number: 2022ZFJH004; National Natural Science Foundation of China, Grant/Award Number: 51925603

Abstract

Biomass gasification combined with CO₂ absorption-enhanced reforming (AER) in a bubbling fluidized bed (BFB) reactor is numerically studied via the multiphase particle-in-cell (MP-PIC) method featuring thermochemical and polydispersity sub-models. A novel bubble detection algorithm is proposed for efficiently characterizing bubble morphology. The effects of several crucial operating parameters on the micro-scale particle behaviors, mesoscale bubble dynamics, and macroscale reactor performance of the AER gasification process are analyzed. Compared with conventional gasification, AER gasification reduces the CO₂ concentration by 33.58% but elevates the H₂ concentration by 32.13%. Higher operating temperature and steam-to-biomass (S/B) ratio promote H₂ generation but deteriorate gasification performance. A lower operating pressure improves gas–solid contact efficiency and gasification performance as the increased operating pressure inhibits bubble dynamics and particle kinematics. Compared with pure sand as bed material, the mixed bed material (CaO:sand = 1:1) significantly improves gasification performance by enhancing H₂ generation and CO₂ removal.

KEYWORDS

biomass gasification, bubbling fluidized bed, CO₂ absorption, multiphase flow, renewable energy

1 | INTRODUCTION

The depletion of fossil fuels and the resulting climate change urge mankind to seek renewable energies. Biomass is becoming a powerful substitute for fossil fuels, with the merits of sustainability, carbon neutrality, and economic feasibility.^{1–4} Gasification is one of the most promising utilization technologies of biomass material, in which the biomass is converted into syngas with high values for subsequent industrial productions. However, the syngas produced by the conventional biomass gasification process usually contains a large amount of CO₂, which will dilute the concentration of combustible gas and reduce the utilization value of the syngas. Besides, the separation of CO₂ from the syngas requires high costs. A feasible method for reducing CO₂ in the syngas is to combine the conventional steam-biomass gasification with CO₂ absorption,⁵ in which the hydrogen is simultaneously enriched.

This process is termed absorption-enhanced reforming (AER) gasification. Calcium oxide (CaO) is commonly employed as a CO₂ absorbent and has received increasing attention due to its low costs and abundant reserves.^{6,7} In the AER gasification process, the generated CO₂ will be absorbed by CaO, thereby changing the equilibrium composition of the syngas and promoting hydrogen production.⁶ Besides, CaO, acting as a tar reforming catalyst, inhibits tar formation and thus improves the total syngas especially hydrogen output.⁸ Therefore, the AER gasification process has become a superior choice for sustainable hydrogen production with CO₂ reduction during biomass utilization.

Bubbling fluidized bed (BFB) is one of the most used reactors for biomass gasification due to its advantages of excellent mixing efficiency, significant heat and mass transfer, good temperature control, and wide fuel flexibility. However, scale-up of the existing lab-scale BFB reactors is still challenging, due to lacking the in-depth

understanding of mesoscale bubble evolution (e.g., generation, coalescence, entrainment), and their relationship with microscale particle behaviors (e.g., segregation, mixing) and macroscale reactor performance (e.g., pressure drop, gas products).⁹ Specifically, the mesoscale bubble structures will “decompose” the gas–solid flow, and the inhomogeneous distribution reduces gas–solid contacts and further affects thermochemical behaviors. The complex multiphase flow and thermochemical behaviors in the BFB reactor present a significant challenge for experimental studies, particularly due to harsh operating conditions and high costs involved.

Numerical simulation provides a cost-effective alternative to the experimental method with the rapid development of computer science. The numerical methods for fluidized bed reactors include Eulerian–Eulerian and Eulerian–Lagrangian methods. The former treats both gas and particle phases as interpenetrating continua and simplifies particle–particle collisions. Thus, this method can be used to predict macro-scale characteristics of the dense particulate system with high efficiency.^{10,11} However, this method cannot identify discrete particle properties (e.g., particle temperature, rotation, and composition). In contrast, the Eulerian–Lagrangian method circumvents the above issues by tracking the trajectory of each particle, computational fluid dynamics–discrete element method (CFD–DEM) and multiphase particle-in-cell (MP–PIC) are the two most representative ones. The CFD–DEM approach tracks each particle individually and resolves particle collisions fully, thus suffering from huge computational resource requirements.¹² This drawback is ameliorated by the MP–PIC approach, which features two advantages: (i) packaging several real particles with the same properties (e.g., size, velocity, specie) into a parcel; (ii) simplifying particle collisions by introducing a solid stress model. By these two strategies, the MP–PIC approach gains a balance between numerical accuracy and calculation efficiency. Moreover, this approach can integrate with heat and mass transfer sub-models for modeling various chemical engineering processes. So far, the MP–PIC approach has been widely applied to investigate biomass gasification in fluidized bed reactors from lab-scale to industrial-scale. Wang et al.¹³ originally investigated biomass gasification in a spouted bed gasifier. They pointed out that biomass particles tend to distribute on the bed surface. Heterogeneous reactions mainly occurred on the bed surface while homogeneous reactions mainly took place in the free-board region. Yang et al.¹⁴ introduced a distribution kernel method into the MP–PIC approach to overcome the numerical stiffness problem caused by the overloading of clustered parcels in the cells. The results showed the new model could satisfactorily capture the transient heat and mass transfer in a lab-scale BFB gasifier. Kong et al.¹⁵ established a reactive MP–PIC model to model biomass gasification in a pilot-scale dual fluidized bed. The results showed that the temperature in the gasifier and the combustor had opposite distribution trends. Yang et al.¹⁶ conducted a state-of-the-art simulation of biomass gasification in a 0.3-MW_{th} pilot-scale circulating fluidized bed and they found that increasing the gas inlet velocity reduced the solids concentration but increased the gas temperature. Kraft et al.¹⁷ numerically simulated biomass gasification in an industrial-scale dual-fluidized bed. The results showed that an inhomogeneous drag model

played a vital role in accurately reproducing pressure drops, temperature distribution, and gas products in a fluidized bed under the fast fluidization regime. The above studies all focus on the macroscale information (e.g., pressure drop, gas products). Nevertheless, the study of mesoscale bubble structures (e.g., generation, coalescence, breakage) during the fluidized bed biomass gasification is still lacking, let alone their relationship with the microscale particle behaviors and macroscale reactor performance. Moreover, to the best of our knowledge, few numerical studies of AER gasification have been reported so far.

Accordingly, the novelty of this study lies in two aspects: (i) developing a reactive MP–PIC model together with an efficient bubble search algorithm for mesoscale bubble characterization; (ii) illuminating the relationship among mesoscale bubble evolution, microscale particle behaviors, and macroscale reactor performance. Moreover, the superiority of the new AER gasification technology is confirmed by comparing it to the conventional biomass gasification technology regarding the lower heating value (LHV) and combustible gas concentration (CGC). The article first gives the mathematical model, followed by numerical settings and grid-independence analysis. After model validation, the effects of several key operating parameters on microscale particle behaviors, mesoscale bubble dynamics, and macroscale reactor performance in the BFB reactor are studied, with a focus on the correlations between mesoscale bubble structures and micro-/macroscale characteristics. The conclusion is presented in the final part.

2 | METHODOLOGY

A large-eddy simulation (LES) model is introduced into the MP–PIC approach for resolving gas turbulence while a solid stress model is employed for simplifying particle collisions. Besides, several particles are packaged into a numerical parcel to reduce particle number. Convection, radiation, and heat of reaction are considered for the heat-transfer process. A shrink core model is used to describe the change in particle diameter due to the heterogeneous reactions. The mathematical model is detailed below.

2.1 | MP–PIC framework

Conservation equations for the gas phase involving mass, momentum, energy, and species are given by^{18,19}:

$$\frac{\partial(\theta_g \rho_g)}{\partial t} + \nabla \times (\theta_g \rho_g \mathbf{u}_g) = \delta \dot{m}_s, \quad (1)$$

$$\frac{\partial(\theta_g \rho_g \mathbf{u}_g)}{\partial t} + \nabla \times (\theta_g \rho_g \mathbf{u}_g \mathbf{u}_g) = -\nabla p_g + \rho_g \theta_g \mathbf{g} + \nabla \times (\theta_g \boldsymbol{\tau}_g) + \mathbf{F}_{gs}, \quad (2)$$

$$\frac{\partial(\theta_g \rho_g h_g)}{\partial t} + \nabla \times (\theta_g \rho_g \mathbf{u}_g h_g) = \theta_g \left(\frac{\partial p_g}{\partial t} + \mathbf{u}_g \cdot \nabla p_g \right) - \nabla \times (\theta_g \mathbf{q}) + S_{gs} + S_{gw} - \Delta H_{rg} + \dot{Q}_D, \quad (3)$$

$$\frac{\partial(\theta_g \rho_g Y_{g,k})}{\partial t} + \nabla \times (\theta_g \rho_g \mathbf{u}_g Y_{g,k}) = \nabla \times (\theta_g \rho_g D \nabla Y_{g,k}) + \delta m_{k,\text{react}}, \quad (4)$$

where ρ_g is the density; \mathbf{u}_g is the velocity vector; p_g is the pressure; θ_g is the volume fraction; \mathbf{g} is the gravitational acceleration. \mathbf{F}_{gs} is the inter-phase momentum exchange term. $\delta \dot{m}_s$ is the source term that links the reaction of discrete phase and continuous phase, which is calculated by integrating the particle distribution function (PDF), as shown in Appendix A. h_g and $Y_{g,k}$ are the enthalpy of the gas mixture and the mass fraction of k th gas species, respectively. $\delta m_{k,\text{react}}$ is the net consumption or production rate of k th gas species. D_g denotes the mass diffusion coefficient. q is the heat flux.

The particle dynamics is denoted by solving the transport equation of f_s as:

$$\frac{\partial f_s}{\partial t} + \nabla \times (f_s \mathbf{u}_s) + \nabla \mathbf{u}_s \times (f_s \mathbf{A}) = \frac{f_D - f_s}{\tau_D}, \quad (5)$$

$$\mathbf{A} = \frac{d\mathbf{u}_s}{dt} = D_s(\mathbf{u}_g - \mathbf{u}_s) - \frac{1}{\rho_s} \nabla p_g - \frac{1}{\theta_s \rho_s} \nabla \tau_s + \mathbf{g} + \frac{\bar{\mathbf{u}}_s - \mathbf{u}_s}{2\tau_D}, \quad (6)$$

where τ_D and \mathbf{A} are the particle damping time and particle acceleration, respectively. $\bar{\mathbf{u}}_s$ represents the mass-averaged solid velocity. τ_s is the particle normal stress, given in Appendix A. The mass and energy conservation equations based on each parcel are given by:

$$\frac{dm_s}{dt} = \sum_{i=1}^N \frac{dm_{s,i}}{dt}, \quad (7)$$

$$m_s C_V \frac{dT_s}{dt} = Q_{sg} + Q_{\text{radi}} - \Delta H_{rs}, \quad (8)$$

where Q_{sg} and Q_{radi} represent the convective heat-transfer flux and radiative heat-transfer flux, respectively. The inter-phase exchange terms are evaluated as:

$$\mathbf{F}_{gs} = - \iiint f_s \left\{ m_s \left[D_s(\mathbf{u}_g - \mathbf{u}_s) - \frac{\nabla p_g}{\rho_s} \right] + \mathbf{u}_s \frac{dm_s}{dt} \right\} dm_s d\mathbf{u}_s dT_s, \quad (9)$$

$$Q_{sg} = \frac{\lambda_g \text{Nu}_s}{d_s} A_s (T_g - T_s), \quad (10)$$

where D_s is the drag function related to solid concentration. The radiative heat flux is given by:

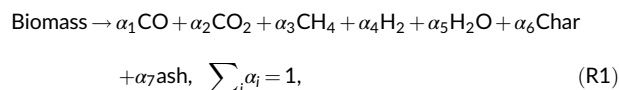
$$Q_{\text{radi}} = \sigma \varepsilon_s A_s (T_{b,\text{local}}^4 - T_s^4), \quad (11)$$

where A_s is the particle surface; σ and ε_s are the Stefan-Boltzmann constant and particle emissivity, respectively. $T_{b,\text{local}}$ and Nu_s are the local environment temperature and particle Nusselt number, respectively. ΔH_{rs} is the heat of the reaction, calculated as the enthalpy difference between products and reactants.

2.2 | Reaction kinetics

In this study, the biomass is pine sawdust.²⁰ Table 1 presents the proximate and ultimate analysis of the biomass.

After entering the reactor, the biomass particles are rapidly heated to a high temperature and pyrolyzed. In this study, the pyrolysis process is described as:



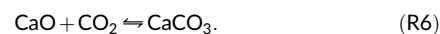
where the α_i is determined according to the proximate and ultimate analysis of the biomass.²¹ As tar is hard to exist at high temperatures, the hydrocarbon is represented by methane. For the convenience of calculation, the elements such as N, S, and Cl are neglected in the present simulation due to their minor amounts. The above assumptions have been widely applied in previous studies.²²⁻²⁴

The reaction kinetics of the pyrolysis process is described by a first-order Arrhenius law^{25,26}:

$$\frac{dm_{\text{volatiles}}}{dt} = -5 \times 10^6 \exp\left(-\frac{1.2 \times 10^8}{RT_p}\right) m_{\text{volatiles}}, \quad (12)$$

where $m_{\text{volatiles}}$ represents the mass of volatiles in the biomass particle. After pyrolysis, the residual char in biomass undergoes a gasification process. Table 2 summarizes the chemical reactions involved in the gasification process and their corresponding reaction rates.²⁷⁻³⁰

In the AER gasification process, CaO carbonation reduces CO_2 concentration, which further affects other parallel reactions and promotes hydrogen generation. The carbonation and calcination reactions of CaO are described as:



The difference between the partial pressure of CO_2 (P_{CO_2}) and the equilibrium partial pressure of CO_2 ($P_{\text{CO}_2,\text{eq}}$) drives the carbonation and calcination reactions in the reactor. $P_{\text{CO}_2,\text{eq}}$ is mainly determined by experiments. Baker³¹ proposed a widely used expression of $P_{\text{CO}_2,\text{eq}}$ as below, with the equilibrium diagram shown in Figure 1.

$$\log_{10} P_{\text{CO}_2,\text{eq}} = 7.079 - \frac{8308}{T}. \quad (13)$$

P_{CO_2} higher than $P_{\text{CO}_2,\text{eq}}$ results in carbonation, whereas P_{CO_2} lower than $P_{\text{CO}_2,\text{eq}}$ results in calcination. These thermodynamic properties determine the temperature range of the AER gasification process. The carbonation reaction requires a temperature ranging from 600 to 700°C, based on a typical CO_2 mole concentration of 10% ~ 20% in the gas products.³²

In this study, the reaction rate of carbonation is based on the correlation proposed by Sun et al.³³:

Ultimate analysis (wt%, dry ash-free basis)				Proximate analysis (wt%, as-received basis)			
C	H	O	N&S	Moisture	Ash	Volatile	Fixed carbon
53.28	5.55	41.15	0.013	6.16	0.53	85.42	7.89

TABLE 1 Proximate analysis and ultimate analysis of the biomass.²⁰

Chemical reaction equation	Chemical reaction rate
Heterogeneous reactions	
R2: $C + H_2O \rightarrow CO + H_2$	$r_2 = A_p p_{H_2O} \frac{r_{diff,2} r_{kin,2}}{r_{diff,2} + r_{kin,2}}$ $r_{kin,2} = 45.6 T_p \exp\left(\frac{4.37 \times 10^7}{RT_p}\right); r_{diff,2} = \frac{5 \times 10^{-12}}{d_p} \left(\frac{T_g + T_p}{2}\right)^{0.75}$
R3: $C + CO_2 \rightarrow 2CO$	$r_3 = A_p p_{CO_2} \frac{r_{diff,3} r_{kin,3}}{r_{diff,3} + r_{kin,3}}$ $r_{kin,3} = 8.3 T_p \exp\left(\frac{4.37 \times 10^7}{RT_p}\right); r_{diff,3} = \frac{5 \times 10^{-12}}{d_p} \left(\frac{T_g + T_p}{2}\right)$
Homogeneous reactions	
R4: $CH_4 + H_2O \rightarrow CO + 3H_2$	$r_4 = 3 \times 10^8 \exp\left(\frac{-1.26 \times 10^8}{RT_g}\right) [CH_4][H_2O]$
R5: $CO + H_2O \leftrightarrow CO_2 + H_2$	$r_5 = (r_{5f} - r_{5b}) / r_{eq}$ $r_{5f} = 2.78 \times 10^3 \exp\left(\frac{-1.26 \times 10^7}{RT_g}\right) [CO][H_2O]$ $r_{5b} = 9.59 \times 10^4 \exp\left(\frac{-4.66 \times 10^7}{RT_g}\right) [CO_2][H_2]$ $r_{eq} = 0.029 \exp\left(\frac{3.40 \times 10^7}{RT_g}\right)$

TABLE 2 Chemical reaction and reaction rates.²⁷⁻³⁰

$$R = 56K_s(1-X)(P_{CO_2} - P_{CO_2,eq})^n S, \quad (14)$$

where n is the reaction order:

$$n = 1, P_{CO_2} - P_{CO_2,eq} \leq 10 \text{ kPa}, \quad (15)$$

$$n = 0, P_{CO_2} - P_{CO_2,eq} > 10 \text{ kPa}, \quad (16)$$

where S is the specific surface area of the CaO particle. K_s is the reaction rate coefficient, given by:

$$K_s = 1.67 \times 10^{-4} \exp\left(\frac{-E}{RT}\right), E = 29 \pm 4 \text{ kJ/mol}, \quad (17)$$

$$P_{CO_2} - P_{CO_2,eq} \leq 10 \text{ kPa},$$

$$K_s = 1.04 \times 10^{-4} \exp\left(\frac{-E}{RT}\right), E = 24 \pm 6 \text{ kJ/mol}, \quad (18)$$

$$P_{CO_2} - P_{CO_2,eq} > 10 \text{ kPa}.$$

2.3 | Bubble search algorithm

An efficient algorithm is developed for bubble characterization. Bubbles will be generated in the BFB reactor when the superficial gas velocity exceeds the minimum fluidization velocity (U_{mf}). The bubble boundary is identified as an iso-surface with a threshold voidage (ϵ_g) of 0.6–0.8.^{34,35} In this work, the voidage of 0.8 is adopted to identify the bubble boundary. Technically, the bubble

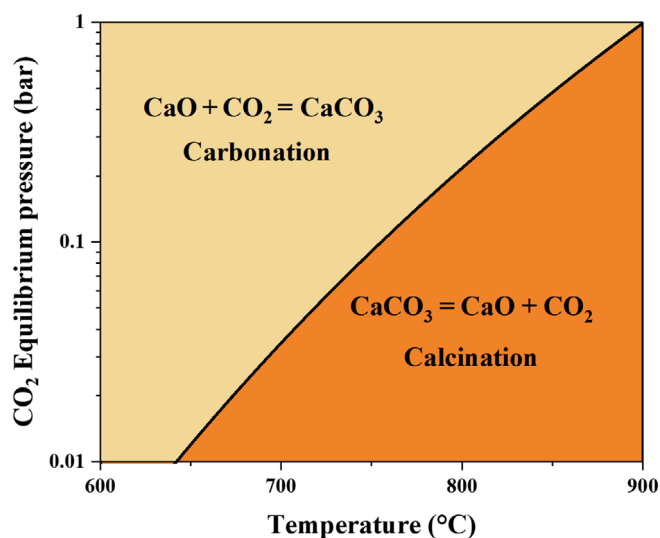


FIGURE 1 The equilibrium diagram of the partial pressure of CO_2 as a function of temperature.³¹

can be represented by many neighboring cells with a voidage larger than the threshold value. The main idea of the bubble search algorithm is illustrated as follows:

1. The computational cells with a voidage larger than 0.8 in the domain are retrieved and put in the vector $Cell_{bub}$.
2. A search process is then performed on each cell in the vector $Cell_{bub}$.

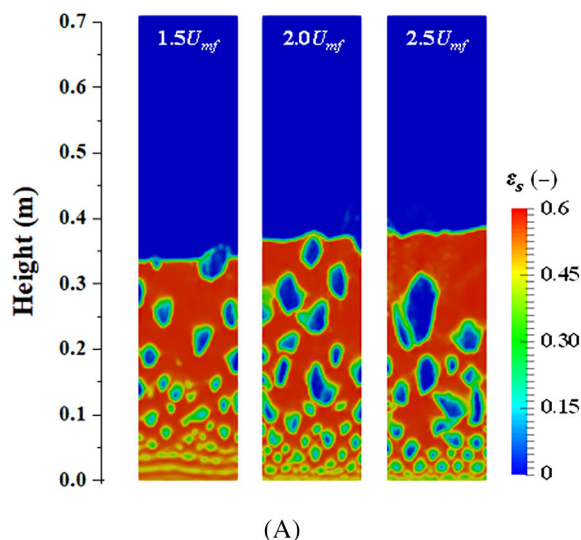
- For cell i in the Cell_{bub} : ① Put the neighboring cells of cell i in Cell_{bub} into the vector Bubi . ② Employ the neighboring cells in the set Bub , as new starting cells to continue searching the corresponding neighboring cells, until the number of cells in the set does not increase. ③ Delete the duplicate cells in the vector Bub .
- In the subsequent searches, the cell will be skipped if cell k has been already contained in a bubble.

Figure 2 shows the schematic representation of the bubble search algorithm. Specifically, the voidage of the cells with the specific label of 35, 36, 37, 43, 44, 45, 51, 52, 53, 27, 28, 29, 19, 21 and 20 reaches the threshold value. Taking cell 44 as the initial one, the neighboring cells 35, 36, 37, 43, 45, 51, 52, and 53 are put into the vector Bub . Continuing searching the neighboring cells based on these known

1	2	3	4	5	6	7	8
9	10	11	12	13	14	15	16
17	18	19	20	21	22	23	24
25	26	27	28	29	30	31	32
33	34	35	36	37	38	39	40
41	42	43	44	45	46	47	48
49	50	51	52	53	54	55	56
57	58	59	60	61	62	63	64
65	66	67	68	69	70	71	72
73	74	75	76	77	78	79	80
81	82	83	84	85	86	87	88

Bubble_{initial} = [44]
 Bubble_{1st iteration} = [35, 36, 37, 43, 44, 45, 51, 52, 53]
 Bubble_{2nd iteration} = [35, 36, 37, 43, 44, 45, 51, 52, 53, 28]
 Bubble_{3rd iteration} = [35, 36, 37, 43, 44, 45, 51, 52, 53, 28, 20]

FIGURE 2 The schematic representation of the bubble search algorithm.



cells, cell 28 meets the requirement and is put into the vector Bub . Similarly, cell 19, 20, 21, 27, 29 is found and put into the vector Bub . After several iterations, the cells that represent the bubble can be found and detailed bubble information can be gained.

Based on the above-mentioned bubble search algorithm, the bubble size is calculated as follows³⁶:

$$d_b = 2 \times \sqrt[3]{3V_b/4\pi}, \quad (19)$$

where V_b is the bubble volume, given by:

$$V_b = \sum_{i=1}^{N_{\text{cell}}} V_{\text{cell},i} \epsilon_{\text{cell},i}, \quad (20)$$

where N_{cell} represents the total amount of cells occupied by the bubble. $V_{\text{cell},i}$ represents the volume of the i th cell, which is the product of the length in the X direction, Y direction, and Z direction of the i th cell. $\epsilon_{\text{cell},i}$ is the voidage of the i th cell.

The central coordinate of the bubble is calculated by averaging the coordinate of all the computational cells occupied by the bubble:

$$C_b = \frac{1}{N_{\text{cell}}} \sum_{i=1}^{N_{\text{cell}}} C_{\text{cell},i}, \quad (21)$$

where C_b is the coordinate of the bubble. $C_{\text{cell},i}$ is the coordinate of the i th cell.

The bubble search algorithm is verified with the experimental measurement by Laverman et al.³⁶ As shown in Figure S1 of Appendix B, the height, width, and thickness of the investigated BFB are 700, 100, and 1.5 mm respectively, with 30, 100, and 1 grids allocated in the X direction, Y direction, and Z direction, respectively. Bed material particles follow a normal size distribution of 400–600 μm , with a density of 2600 kg/m^3 . At the initial time, the height of the

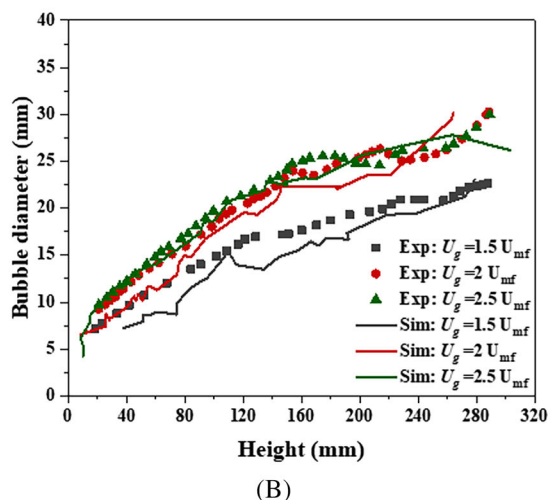


FIGURE 3 (A) Spatial distribution of bubbles at different inlet velocities; (B) comparison of the predicted bubble diameter with the experimental data.

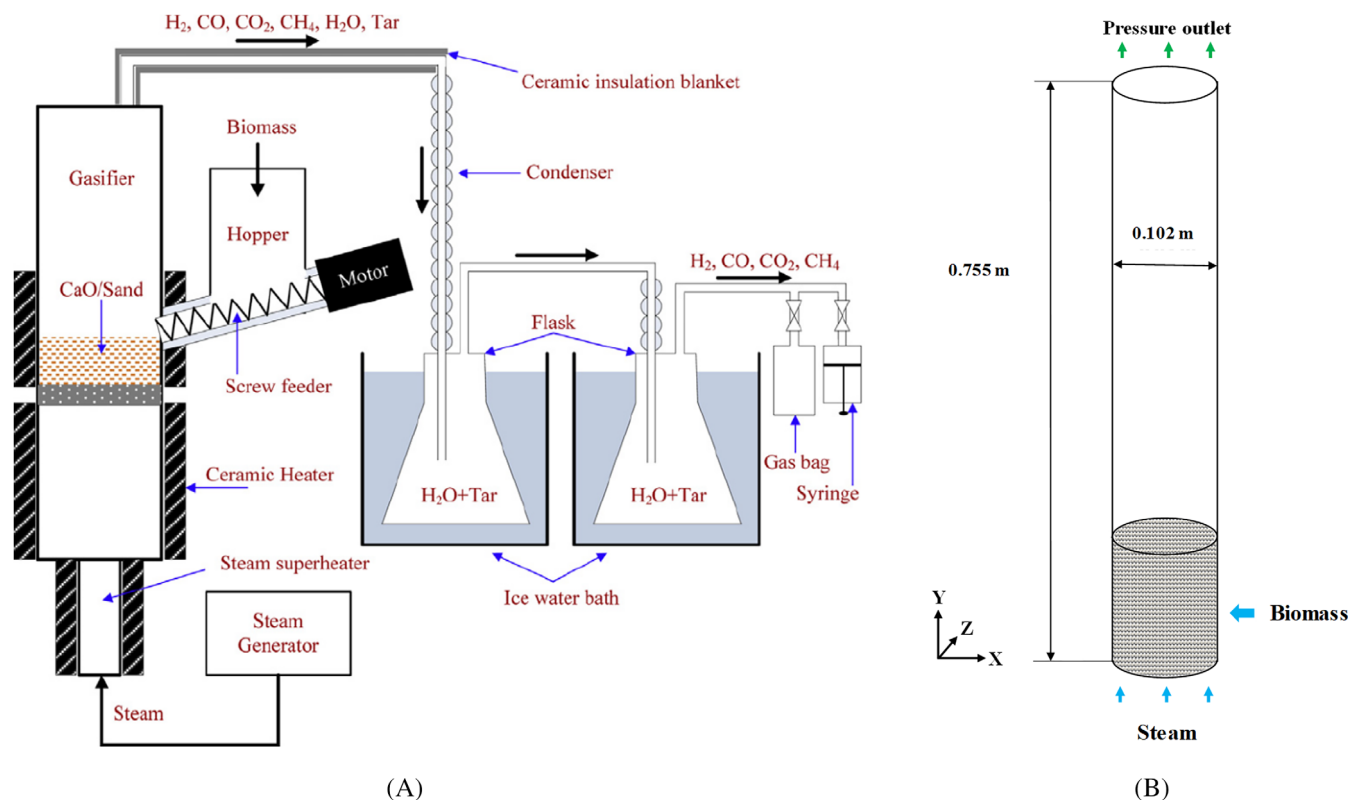


FIGURE 4 (A) Experimental setup²⁰; (B) the investigated BFB reactor in the simulation.

TABLE 3 Chemical composition of calcined limestone (wt%).

CaO	MgO	SiO ₂	Fe ₂ O ₃	Al ₂ O ₃	CaCO ₃
95.5	0.9	1.3	0.2	0.4	1.1

packed bed is 0.3 m. Airflow is introduced from the bottom at 25°C. The U_{mf} is 0.18 m/s. Three groups of inlet velocities are assigned consistent with the experiment settings, that is, $1.5 U_{mf}$, $2.0 U_{mf}$, $2.5 U_{mf}$. Figure 3A illustrates the spatial distribution of bubbles at different inlet velocities. Small bubbles are generated at the bottom and coalesce with each other to form large bubbles in the rising process, causing a decrease in bubble number. With the increase in inlet velocity, the bubble volume also increases significantly. Figure 3B shows the comparison between predicted values and experimental data on the relationship between bubble diameter and axial position at different inlet velocities. At low inlet gas velocities (i.e., $1.5 U_{mf}$, $2.0 U_{mf}$), the developed bubble search algorithm can well capture the variation trend of bubble volume as a function of the height. At high inlet gas velocity ($2.5 U_{mf}$), opposite trends of the numerical results and experimental data at the bed height over 260 mm are observed. According to the bubble search algorithm, the bubble volume is calculated by counting the volume of computational cells with a voidage of greater than 0.8 in a closed region. In the BFB, the bubble diameter under different inlet gas velocities typically increases with the bed height. At low inlet gas velocities (i.e., $1.5 U_{mf}$, $2.0 U_{mf}$), the evolution of the bubbles is regular, with clear boundaries and easy to distinguish. At a high inlet gas velocity (i.e., $2.5 U_{mf}$), the evolution of the bubbles is violent,

TABLE 4 Detailed gas–solid and operating parameters in the simulation.

Parameters	Value	Unit
Bed size (height/diameter)	0.755/0.102	m
Particle size (sand/CaO/biomass)	0.25 ~ 0.3/0.25 ~ 0.3/0.42 ~ 0.5	mm
Particle density (sand/CaO/biomass)	2300/1600/660	kg/m ³
Particle temperature (biomass)	27	°C
Operating temperature	550, 600, 650, 700	°C
Operating pressure	0.5, 1, 1.5, 2	MPa
Steam-to-biomass ratio	1.47, 2.29, 3.41, 3.91	-
Inlet steam flow rate	1.26	kg/h
Steam temperature	200	°C
Solid volume fraction at close pack	0.58	-
Particle normal-to-wall retention coefficient	0.9	-
Particle tangential-to-wall retention coefficient	0.3	-
Fraction coefficient	0.3	-
Time step	1.0×10^{-5}	s

and the bubbles break up before reaching the bed surface, leading to cavities with high voidage that cannot be counted in the calculation of the bubble volume. Accordingly, the time-averaged bubble volume at the upper part of the bed (i.e., $h > 260$ mm) is smaller than the

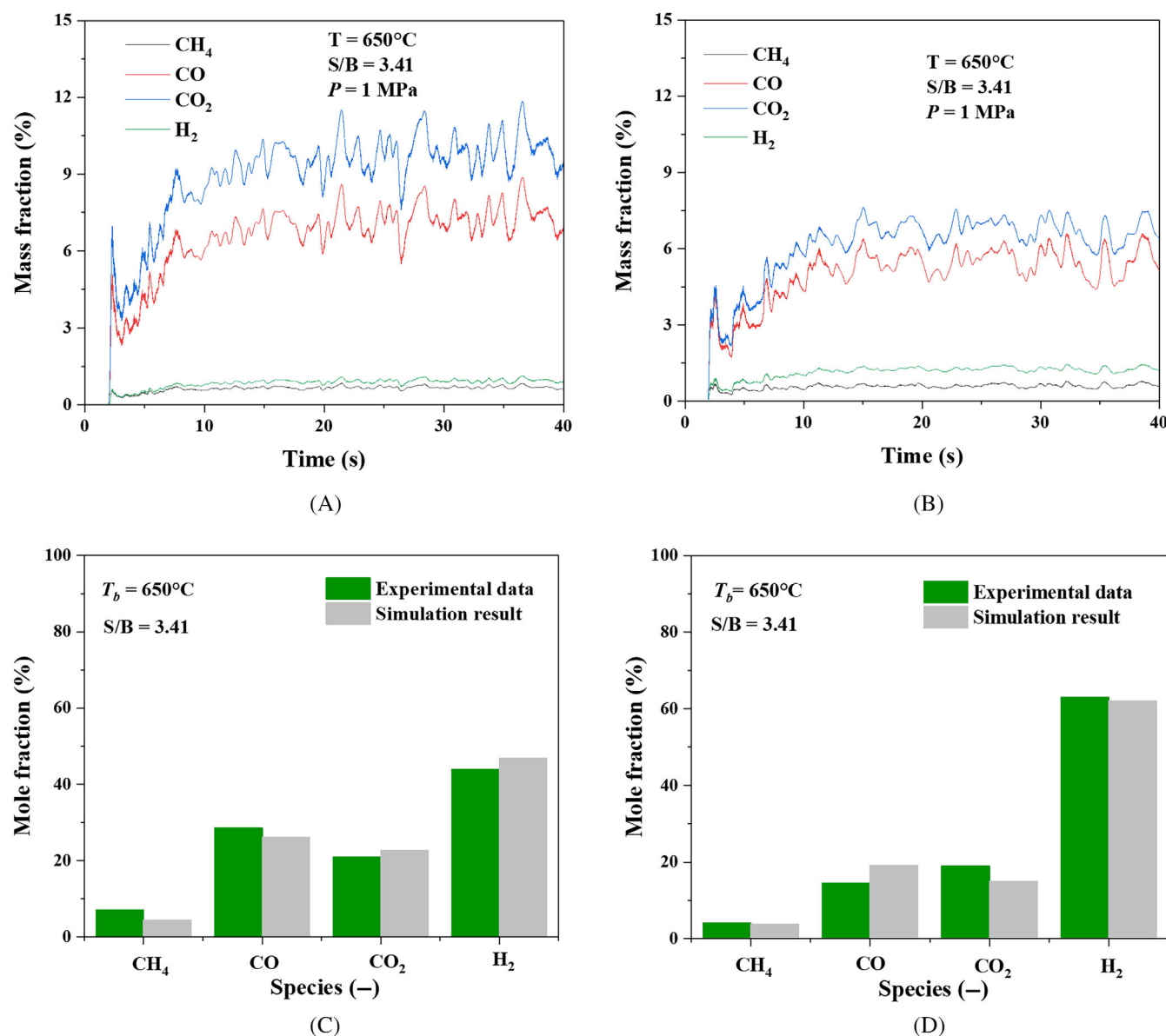


FIGURE 5 Model validation regarding the gas products obtained at the reactor exit: (A) time-evolution of mass fractions in the conventional gasification; (B) time-evolution of mass fractions in the AER gasification; (C) time-averaged mass fractions in the conventional gasification; (D) time-averaged mass fractions in the AER gasification.

experimental data with an opposite tendency. Despite the slight discrepancy between numerical results and experimental data under the specific condition and region, the prediction of bubble dynamics using the proposed bubble search algorithm is reasonable and acceptable for most operating conditions.

3 | SIMULATION CONDITIONS

3.1 | Numerical settings

The investigated object is a lab-scale BFB reactor, consistent with the experimental test rig used by Udomsirichakorn et al.²⁰ (Figure 4A). As shown in Figure 4B, the height and inner diameter of

the reactor are 755 and 102 mm, respectively. 683 g sand or 488 g calcined limestone is used as bed material. Particles have a normal size distribution of 0.25–0.3 mm. Table 3 lists the composition of limestone (hereinafter referred to as CaO). Non-slip and constant temperature boundary conditions are applied to the walls. Biomass particles are fed from the side of the reactor, and superheated steam is introduced from the bottom. Before the gasification process, the reactor is first heated up to the operating temperature (e.g., 650°C) and maintained at the operating pressure. In the simulation, the wall temperature is set as a fixed value (i.e., $T_b = 550, 600, 650,$ and 700°C) to maintain the temperature in the reactor and provide additional heat for the gasification process. The operating pressure in the reactor is maintained by constant inlet and outlet pressures in the gasification process.

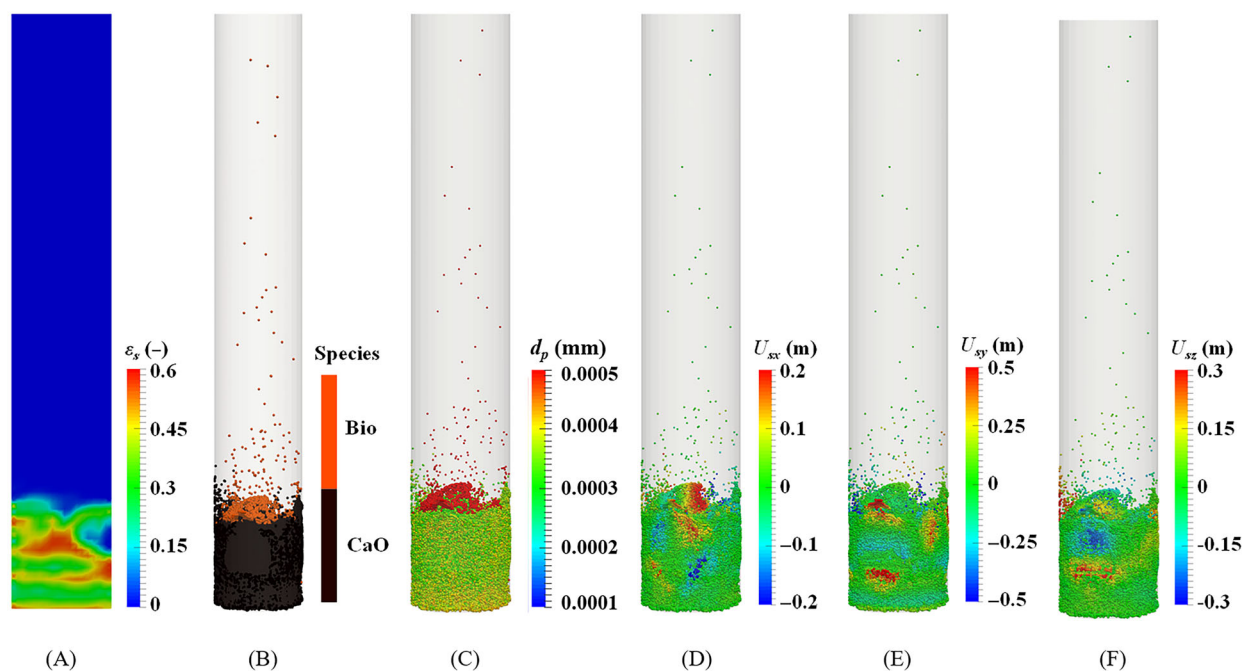


FIGURE 6 General flow pattern in the BFB reactor under the AER gasification condition at $t = 30$ s: (A) solid holdup; (B) solid species; (C) particle diameter; (D) U_{ax} ; (E) U_{ry} ; (F) U_{sz} . (Note that the particle size is enlarged for better visualization).

The base case is operated at an operating temperature of 650°C , an operating pressure of 1 MPa, and a S/B ratio of 3.41. In addition, the effects of different operating parameters (e.g., operating temperature, operating pressure, S/B ratio, bed material) on the hydrodynamics and thermochemical behaviors of the conventional and AER gasification processes are explored. Table 4 lists the detailed gas–solid and operating parameters.^{17,37,38}

3.2 | Grid-independence analysis

Three groups of grids, i.e., 17,407 grids (i.e., coarse grids), 26,550 grids (i.e., medium grids), and 45,360 grids (i.e., fine grids) are specified to test the grid independence. The spatial distribution of time-averaged pressure and temperature, which can reflect the gas–solid flow quality and thermochemical behaviors in the BFB reactor, are used as two indicators to characterize grid independence. As shown in Figure S2 of Appendix B, the medium and fine grids have similar pressure and temperature distributions, but coarse grids differ significantly from the others. Based on the consideration of both numerical accuracy and computational efficiency, the medium grids are adopted in the following simulations.

4 | RESULTS AND DISCUSSION

4.1 | Model validation

Figure 5A,B illustrates the time-evolution profiles of the concentration of gas products obtained at the reactor exit of the conventional and

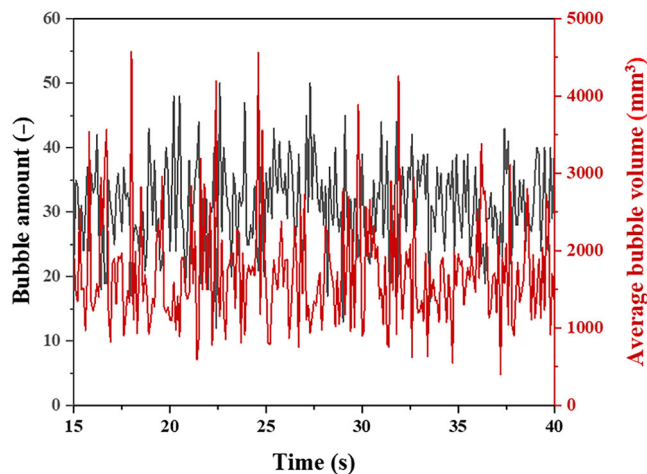


FIGURE 7 Time-evolution profiles of bubble amount and average bubble volume in the BFB reactor.

AER gasification processes. Specifically, in the conventional gasification process, pure sand is used as bed material, the operating temperature is 650°C , the S/B is 3.41, and the operating pressure is 1 MPa. In the AER gasification processes, pure CaO is adopted as bed material, and the operating temperature, the S/B, and the operating pressure are consistent with that in the conventional gasification process. Compared with conventional gasification, AER gasification significantly reduces CO_2 concentration but improves H_2 concentration. After 15 s, the mass fraction of gas products fluctuates around fixed values under two scenarios, suggesting that the system has reached a steady state. Accordingly, the data after 15 s are taken for time averaging.

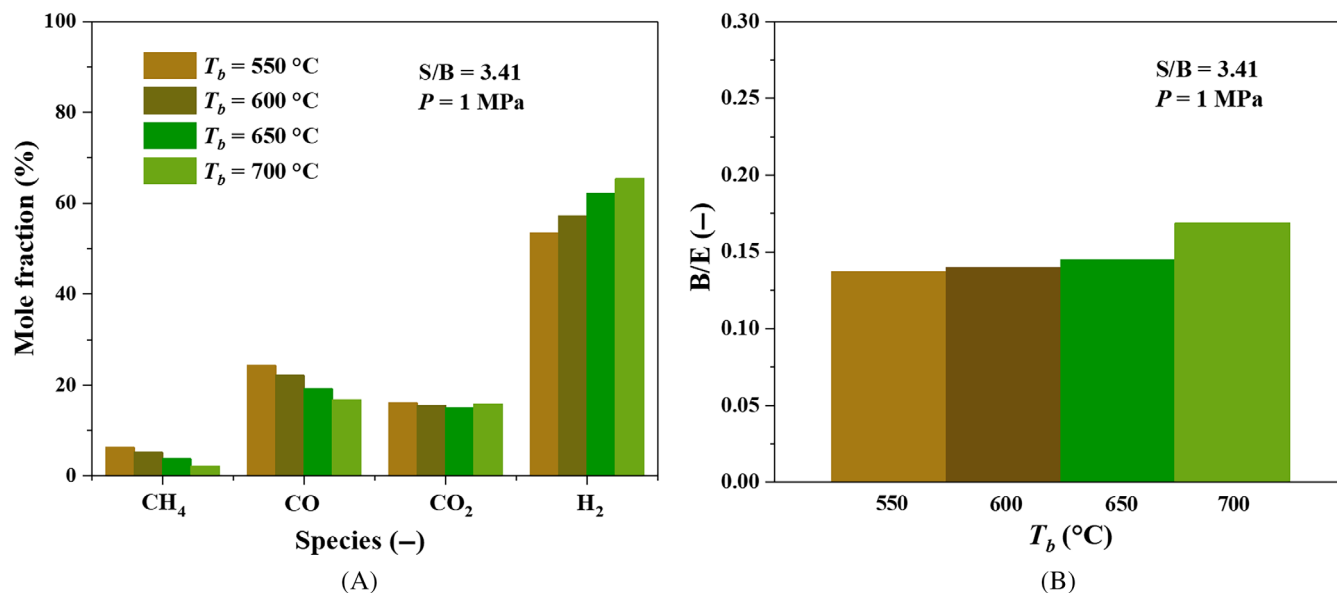


FIGURE 8 Effect of operating temperature on the concentration of gas species (A) and B/E ratio (B).

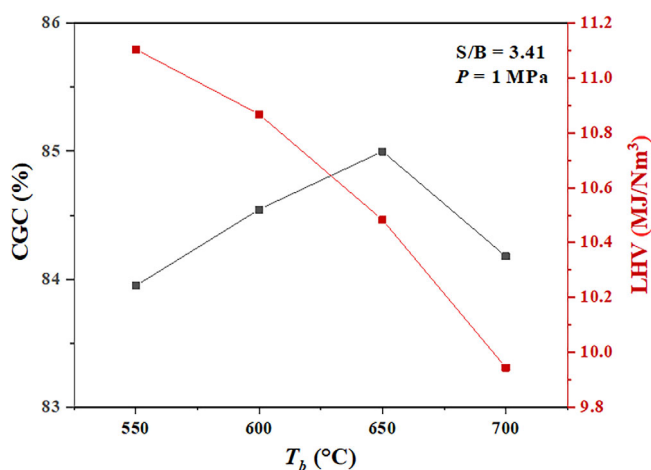


FIGURE 9 Effect of operating temperature on the LHV and CGC.

Figure 5C,D shows the comparison between the numerical results and experimental data under the conventional and AER gasification processes. As shown in the figure, the predicted concentration of the gas species shows slight discrepancies with experimental data. In the gasification process, hundreds of homogeneous and heterogeneous reactions take place simultaneously in the reactor, and it is impractical to implement the detailed reaction kinetics in the model. Therefore, the chemical reactions are simplified into several global reactions. Moreover, reaction kinetics dominate the thermochemical behaviors in the reactor, which have various values according to different literature.^{39–41} The discrepancies between numerical results and experimental data are inevitable but acceptable. Hence, the present model can reasonably predict the thermochemical properties of both the conventional and AER gasification processes in the BFB reactor.

Two indicators, lower heating value (LHV) and combustible gas (i.e., H₂, CO, CH₄) concentration (CGC), are adopted to evaluate the gasification performance. The LHV of the gas products is defined as²³:

$$\text{LHV} \left(\text{MJ/Nm}^3 \right) = (25.7 \times \text{H}_2\% + 30.3 \times \text{CO}\% + 85.4 \times \text{CH}_4\%) \times (4.2/1000). \quad (22)$$

The CGC is defined as¹⁵:

$$\text{CGC}(\%) = \frac{\text{The volume summation of H}_2, \text{ CO, and CH}_4 \text{ in syngas}}{\text{Total volume of syngas (without H}_2\text{O)}} \times 100\%. \quad (23)$$

Compared with conventional gasification, AER gasification reduces the CO₂ concentration by 33.58% but elevates the H₂ concentration by 32.13%. For the conventional and AER gasification processes, the LHV is respectively 9.94 and 10.483 MJ/Nm³ while the CGC is respectively 77.41% and 85%. The gas quality is considerably improved by AER gasification. Specifically, the absorption of CO₂ by CaO causes the balance of the corresponding parallel reactions (i.e., R4 and R5) to shift toward the forward reaction direction, resulting in a corresponding change in the concentration of the gas products.

4.2 | General flow pattern

Gas–solid flow hydrodynamics significantly affects the thermochemical characteristics and overall performance of the BFB reactor. Figure 6 illustrates the general flow pattern under the AER gasification condition at $t = 30$ s. Particles are fluidized by the introduced steam flow, and several bubbles are observed in the dense phase region. Bubbles dominate the gas–solid flow, affect the gas–particle/particle–particle mixing,

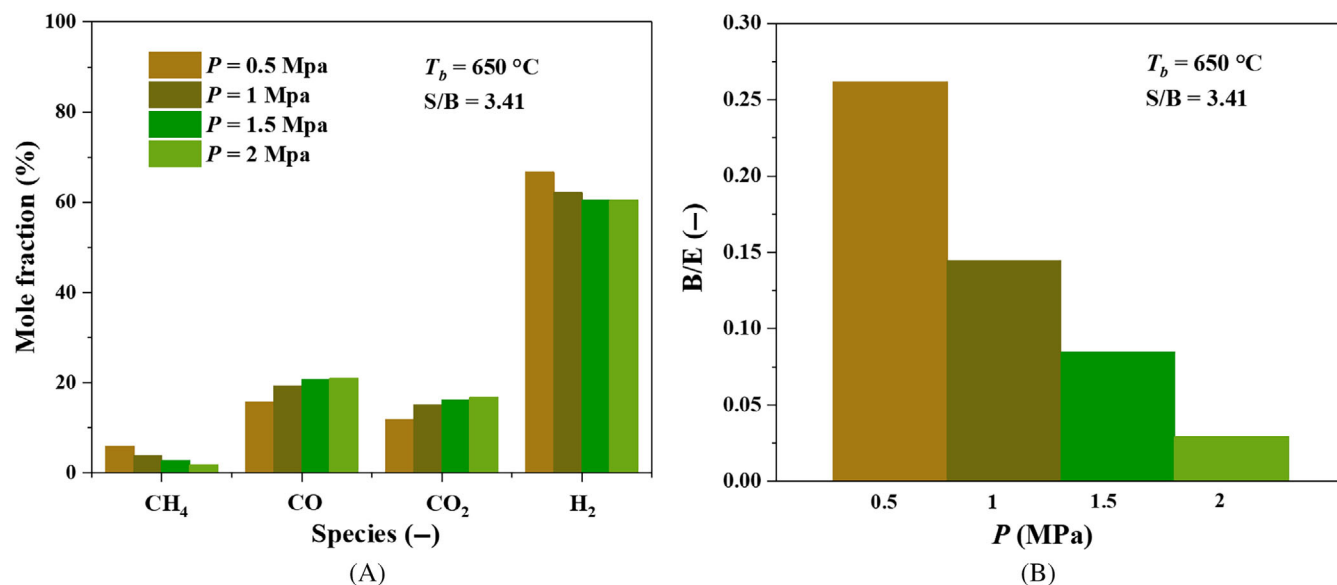


FIGURE 10 Effect of operating pressure on the concentration of gas species (A) and B/E ratio (B).

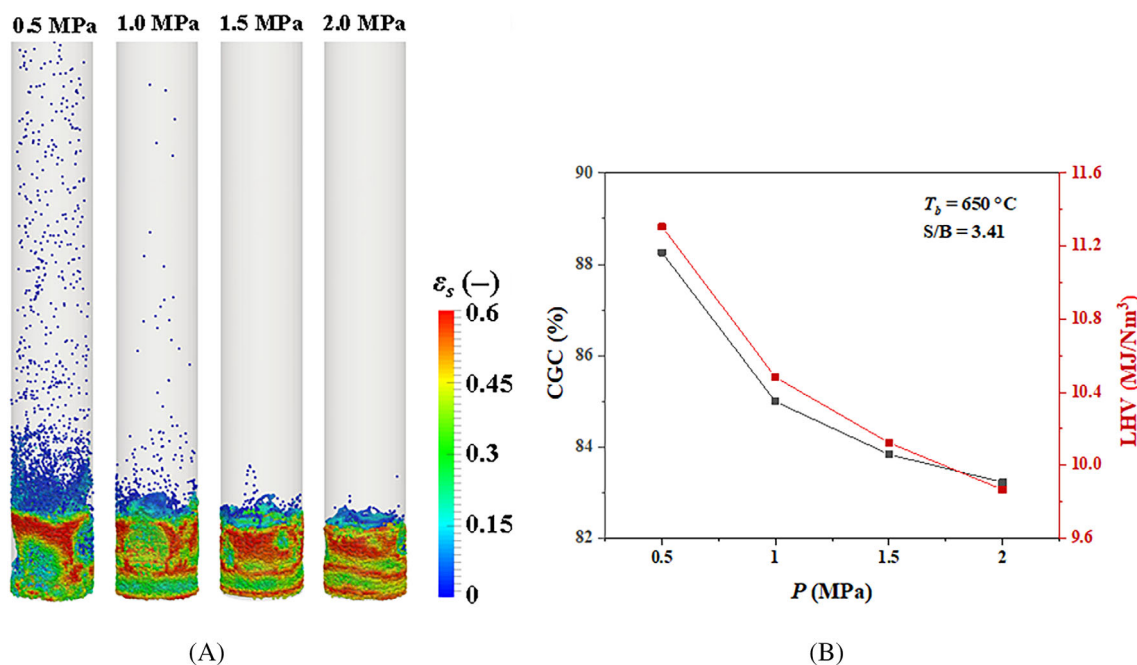


FIGURE 11 Effect of operating pressure on the flow pattern (A) and the CGC and LHV (B).

and determine flow regimes and the resulting fluidization quality. Besides, the distribution of bubbles greatly affects the spatial distribution of temperature, gas component concentration, and reaction rate, thereby determining the overall reactor performance.

Due to the density and mass difference, significant particle segregation is observed in the bed. Lighter biomass particles are distributed on the bed surface. As the reactions proceed, the continuous mass loss leads to the size reduction of biomass particles, which are then carried up by the gas flow and finally escape from the exit. Due

to the dominant role of the vertically introduced steam flow, vigorous vertical particle velocity (U_{sy}) is observed in the BFB. Horizontal migration of particles (U_{sx} , U_{sz}) is also observed, which results from the combined effect of inter-particle/phase interactions and bubble evolution.

Figure 7 gives the time-evolution profiles of bubble amount and average bubble volume in the BFB reactor after $t = 15$ s. The profiles fluctuate around constants over time, corresponding to the generation, coalescence, and breakage of the bubbles. Moreover, the time-

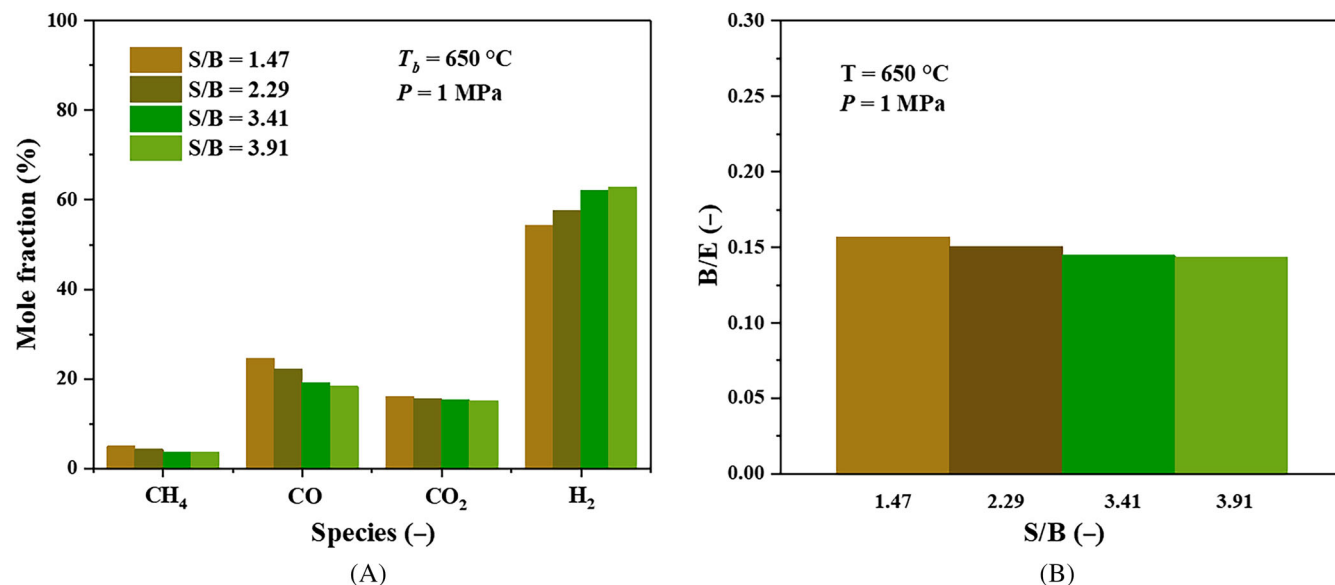


FIGURE 12 Effect of the S/B ratio on the concentration of gas species (A) and B/E ratio (B).

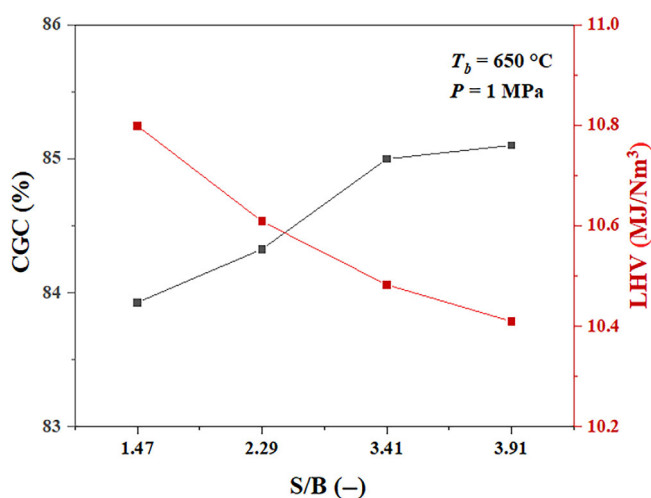


FIGURE 13 Effect of the S/B ratio on the CGC and LHV.

evolution trend of bubble amount and bubble volume is opposite, and a large bubble volume corresponds to a small bubble amount.

4.3 | Effect of operating temperature

This section studies the effect of operating temperature (T_b) on the AER gasification process. As shown in Figure 8A, increasing the operating temperature improves the H_2 concentration from 53.4% to 65.3%, which is mainly attributed to the promotion of methane-steam reforming reaction (R4) and water-gas shift reaction (R5). This point is convinced by the decrease of CO and CH_4 concentrations with temperature. Specifically, the CO concentration decreases from 24.27% to 16.7% while the CH_4 concentration decreases from 6.28% to

2.13%. The CO_2 concentration decreases with the increase in temperature but increases when the temperature exceeds $650\text{ }^\circ\text{C}$. This can be associated with the enhancement of the water-gas shift reaction at high temperatures, which produces a large amount of CO_2 . Figure 8B shows the volume ratio of the bubble phase to the emulsion phase (i.e., B/E ratio) in the BFB under different operating temperatures, and the emulsion phase refers to a region with a solid holdup higher than 0.2. The B/E ratio positively correlates with the operating temperature. According to $PV = nRT$, the gas expands at high temperatures. Besides, a higher temperature promotes chemical reactions, which also leads to a change in the gas volume in the bed.

Figure 9 illustrates the effect of operating temperature on the CGC and LHV. Increasing operating temperature decreases the LHV from 11.1 to $9.94\text{ MJ}/\text{Nm}^3$, as CH_4 concentration with a high heat value decreases with the increased operating temperature. From $550\text{ }^\circ\text{C}$ to $650\text{ }^\circ\text{C}$, the CGC increases from 83.95% to 85% but decreases to 84.18% when the operating temperature exceeds $650\text{ }^\circ\text{C}$, which is due to the increased CO_2 concentration in the gas products.

4.4 | Effect of operating pressure

The effect of the operating pressure (P) on the AER gasification process is given in Figures 10 and 11. Increasing operating pressure decreases H_2 concentration from 66.64% to 60.42% but increases CO_2 concentration from 11.74% to 16.77%. Accordingly, CH_4 concentration decreases from 5.89% to 1.82%, while CO concentration increases from 15.73% to 20.99%. Besides, as the operating pressure elevates, the B/E ratio drops sharply, leading to gentle gas-solid motions. According to $PV = nRT$, the gas expands at a lower pressure, and larger-size bubbles lead to more intense gas-solid motions. The

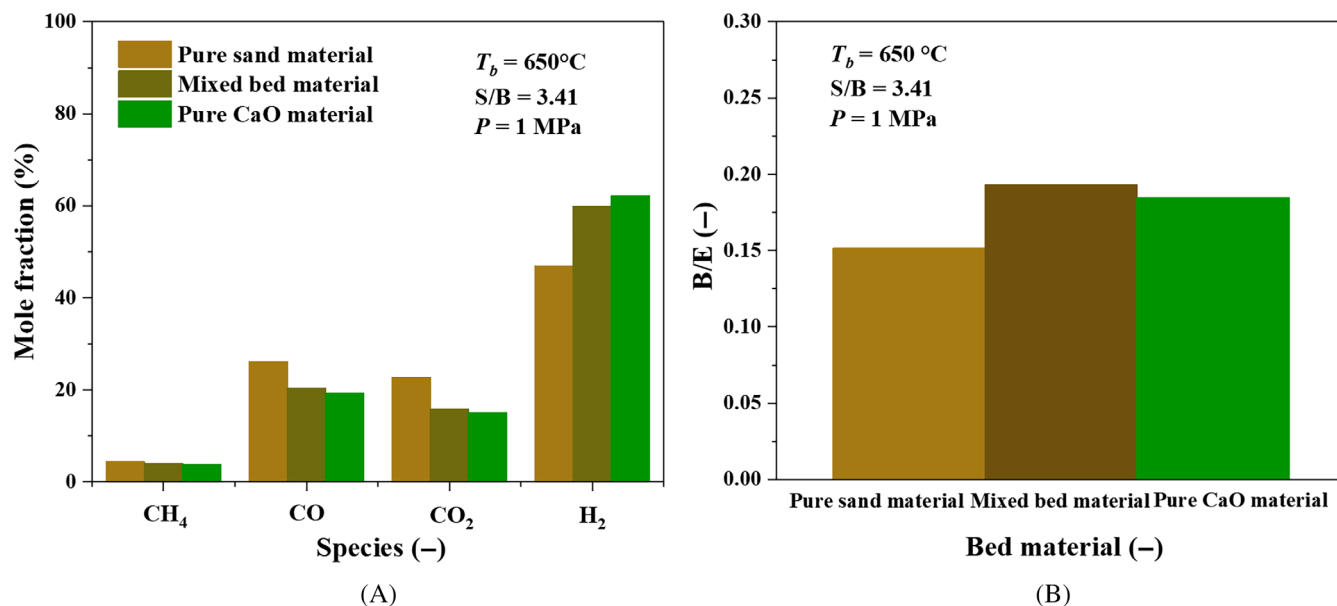


FIGURE 14 Effect of bed material on the concentration of gas species (A) and B/E ratio (B).

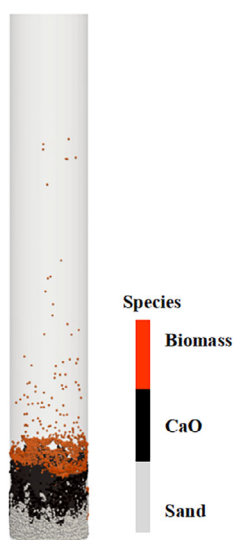


FIGURE 15 Density-induced segregation in the BFB reactor with the mixed bed material (CaO:sand = 1:1). (Note that the particle size is enlarged for better visualization).

intense gas–solid motions further strengthen particle–gas/particle mixing, which enhances the carbonization reaction and related parallel reactions. The decrease in CO and CO_2 concentrations can support this conclusion. CH_4 concentration decreases with the increase in operating pressure, owing to the higher H_2 concentration under a lower operating pressure inhibiting the methane–steam reforming reaction (R4). Increasing operating pressure inhibits bubble evolution and particle kinematics, deteriorating gas–solid mixing and chemical reactions.

As illustrated in Figure 11B, increasing operating pressure from 0.5 to 2 MPa decreases the LHV from 11.31 to 9.85 MJ/Nm³ and

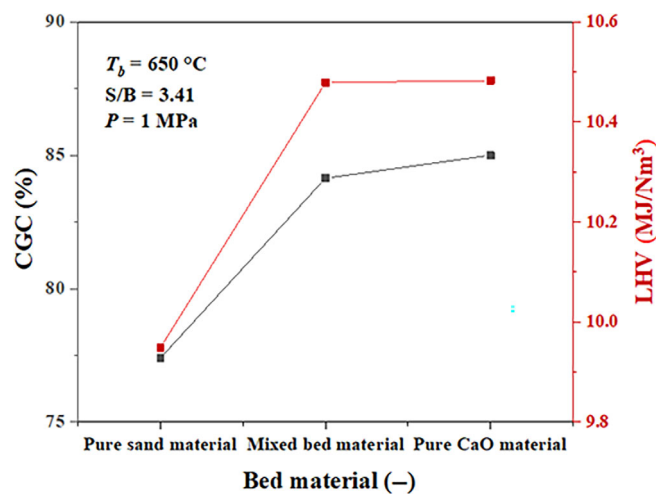


FIGURE 16 Effects of bed material on the CGC and LHV.

decreases the CGC from 88.26% to 83.23%. The decrease in the LHV and CGC as the pressure increases indicates that the gas product quality decreases under higher pressure, and a lower operating pressure benefits AER gasification.

4.5 | Effect of steam to biomass ratio

Figure 12 illustrates the effect of the steam to biomass (S/B) ratio on the concentration of gas species and the B/E ratio under the AER gasification condition. To avoid affecting bed hydrodynamics, varying the S/B ratio is achieved by varying the feeding rate of biomass. As shown in Figure 12A, with the increase in the S/B ratio, H_2 concentration increases from 54.3% to 63.17%, and CO_2 concentration decreases

from 16.07% to 14.9%. A higher S/B ratio promotes methane-steam reforming reaction and water-gas shift reaction, thus increasing H₂ concentration but decreasing CH₄ and CO concentrations. A lower S/B ratio results in more biomass particles entering the reactor, producing more CO₂ during the gasification process, thus the CO₂ concentration is slightly higher at a lower S/B ratio. As the S/B ratio increases, the mass of biomass particles entering the reactor and the total volume of gas generated by chemical reactions all decrease, leading to the reduction of the B/E ratio at the increased S/B ratio. The effect of the S/B ratio on the CGC and LHV is illustrated in Figure 13. As the S/B ratio increases, the LHV decreases from 10.8 to 10.41 MJ/Nm³ due to the decrease in CH₄ and CO concentrations, and the CGC increases from 83.93% to 85.1% as a result of the decrease in CO₂ concentration.

4.6 | Effect of bed material

Three groups of bed materials with different compositions are assigned to study their effects on the AER gasification process, i.e., pure sand, mixed bed material (CaO: sand = 1: 1), and pure CaO. Figure 14A shows the concentration of gas species with different bed materials. Compared with the bed material of pure sand, the mixed bed material and the bed material of pure CaO significantly increase H₂ concentration and significantly decrease CO₂ concentration. Besides, the absorption of CO₂ by CaO shifts the corresponding parallel reactions (i.e., R4 and R5) toward the forward reaction direction. Therefore, the mixed bed material and the bed material of pure CaO reduce the concentrations of CH₄ and CO. The mixed bed material has an insignificant difference in the concentration of gas species with the pure CaO material. The reason for this is illustrated in Figure 15. In the case of mixed bed material, significantly density-induced particle segregation appears in the reactor. Specifically, sand particles with a higher density are deposited in the bottom part, CaO particles reside above the sand material, and biomass particles with a lower density are distributed on the bed surface. This makes sufficient contact between CaO particles and the gases generated by chemical reactions and ensures the progress of the carbonization reaction. Figure 14B illustrates the effects of bed material on the B/E ratio. Compared with pure sand material, the mixed bed material significantly improves the B/E ratio. CaO absorbs CO₂ and promotes the methane-steam reforming reaction (R4). The gas volume expansion increases the B/E ratio. However, the B/E ratio in the bed with the pure CaO material is smaller than that with the mixed bed material, owing to the particle segregation phenomenon in the latter.

Figure 16 shows the variation of LHV and CGC with different bed materials. With the mixed bed material, the increase in the concentration of H₂ and the decrease in the concentration of CO₂ indicates the improvement of gasification performance. Although the mixed bed material reduces the concentrations of CH₄ and CO, the reduction of them insignificantly affects gasification performance due to the tiny proportion of CH₄ and CO in the gas products. Specifically, compared with the bed material of pure sand, the mixed

bed material increases the LHV from 9.94 to 10.48 MJ/Nm³ and increases the CGC from 77.41% to 84.14%, showing a significant improvement in gasification performance. With the bed material of pure CaO, the increase in the proportion of CaO slightly improves gasification performance due to the density-induced particle segregation. The particle segregation phenomenon results in a lower particle mixing degree and a reduced intra-phase or inter-phase contact efficiency, thus inhibiting the carbonation reaction. Specifically, compared with the mixed bed material, the bed material of pure CaO increases the LHV from 10.48 to 10.483 MJ/Nm³ and increases the CGC from 84.14% to 85%, showing a slight improvement in gasification performance.

5 | CONCLUSION

In this study, the AER gasification process in a BFB reactor is numerically studied via the MP-PIC approach, with a focus on mesoscale bubble behaviors. A novel bubble search algorithm is developed for bubble characterization. The effects of several key operating parameters (i.e., operating temperature, operating pressure, S/B ratio, and bed material) on microscale particle behaviors, mesoscale bubble dynamics, and macroscale reactor performance of the AER gasification process are investigated. The conclusions can be drawn as follows:

1. The reaction kinetics considering carbonation and calcination are confirmed to be reasonable to describe the conventional and AER gasification processes in the BFB reactors. Compared with conventional gasification, AER gasification reduces the CO₂ concentration by 33.58% but elevates the H₂ concentration by 32.13%. For the conventional and AER gasification processes, the LHV is respectively 9.95 and 10.483 MJ/Nm³ while the CGC is respectively 77.41% and 85%, demonstrating the improvement of gas quality by the AER gasification technology.
2. A high operating temperature promotes H₂ generation and CO₂ removal but will increase the CO₂ generation when the operating temperature exceeds 650°C. A higher operating temperature deteriorates the AER gasification process.
3. A lower operating pressure improves gas-solid contact efficiency and H₂ generation by strengthening bubble dynamics and particle kinematics. Increasing operating pressure from 0.5 to 2 MPa decreases the LHV from 11.31 to 9.85 MJ/Nm³, and decreases the CGC from 88.26% to 83.23%, demonstrating that a lower operating pressure benefits gasification performance.
4. Increased S/B ratios result in a higher H₂ concentration and a reduced CO₂ concentration. In addition, a high S/B ratio decreases the LHV but increases the CGC. Compared with pure sand as bed material, the mixed bed material (CaO:sand = 1:1) significantly improves the gasification performance in terms of enhancing H₂ generation and CO₂ removal. Due to the influence of particle segregation, further increasing the proportion of CaO in the bed material insignificantly improves gasification performance.

In the AER gasification process, inter-particle collisions and particle segregation lead to the fragmentation of CaO particles and the decrease of contact efficiency, respectively, which call for the design of wear-resistant Ca-based adsorbents and the optimization of fluidized bed reactors.

NOMENCLATURE

A	particle acceleration (m/s^2)
A_s	particle surface area (m^2)
C_V	specific heat capacity of particle ($\text{J}/[\text{kg}\cdot\text{K}]$)
C	model constant (-)
D_g	mass diffusion coefficient of gas (m^2/s)
D_s	drag function coefficient (-)
d_s	particle diameter (m)
h_g	enthalpy (J/kg)
f_s	distribution function of particle (-)
F_{gs}	interphase force between the gas and particle phases (N/m^3)
g	gravitational acceleration (m/s^2)
ΔH_r	heat source forming from chemical reactions (W/m^3)
m	mass (kg)
$\delta\dot{m}_s$	mass source term ($\text{kg}/[\text{m}^3\cdot\text{s}]$)
$\delta m_{k,\text{react}}$	the net consumption or production rate of k th gas species ($\text{kg}/[\text{m}^3\cdot\text{s}]$)
Nu	Nusselt number (-)
p	pressure force (N)
P_s	pressure constant (Pa)
Pr_t	turbulent Prandtl number (-)
q	heat flux (W/m^2)
Q_{sg}	the convective heat-transfer flux (W)
Q_{radi}	the radiative heat-transfer flux (W)
\dot{Q}_D	enthalpy diffusion term (W/m^3)
Re	Reynolds number (-)
S_{gs}, S_{gw}	energy exchange term (W/m^3)
T	temperature (K)
u	velocity (m/s)
$Y_{g,k}$	mass fraction of gas species k (-)

GREEK SYMBOLS

θ	volume fraction (-)
ε_s	particle emissivity
δ_{ij}	unit tensor (-)
λ_{mol}	the molecular conductivity of the gas phase ($\text{W}/[\text{m}\cdot\text{K}]$)
λ_t	the turbulent conductivity of the gas phase ($\text{W}/[\text{m}\cdot\text{K}]$)
ρ	density (kg/m^3)
τ_D	particle collision damping time (s)
τ_g	fluid stress tensor (Pa)
μ_t	turbulent viscosity ($\text{kg}/[\text{m}\cdot\text{s}]$)
μ_l	laminar viscosity ($\text{kg}/[\text{m}\cdot\text{s}]$)
μ	shear viscosity ($\text{kg}/[\text{m}\cdot\text{s}]$)
τ_s	inter-particle stress (Pa)
θ_{cs}	particle volume fraction at close packing (-)

Δ	sub-grid length scale (m)
σ	Stefan-Boltzmann constant (-)
β, α	model constant (-)

SUBSCRIPTS

g	gas phase
s	particle phase
i, j	coordinate index

ACRONYMS

BFB	bubbling fluidized bed
CFD	computational fluid dynamics
DEM	discrete element method
MP-PIC	multiphase particle-in-cell

AUTHOR CONTRIBUTIONS

Dali Kong: Conceptualization (lead); data curation (lead); investigation (lead); methodology (lead); validation (equal); writing – original draft (lead); writing – review and editing (lead). **Shuai Wang:** Conceptualization (lead); data curation (equal); investigation (equal); project administration (lead); resources (lead); software (lead); validation (equal); writing – original draft (equal); writing – review and editing (lead). **Kun Luo:** Conceptualization (lead); funding acquisition (lead); project administration (lead); resources (lead). **Jianren Fan:** Funding acquisition (lead); project administration (lead); resources (lead).

ACKNOWLEDGMENTS

We acknowledged the support from the National Natural Science Foundation of China (No. 51925603) and the Fundamental Research Funds for the Central Universities (2022ZFH004).

CONFLICT OF INTEREST STATEMENT

The authors declare no conflicts of interest.

DATA AVAILABILITY STATEMENT

The data that support the findings of this study are available from the corresponding author upon reasonable request.

ORCID

Shuai Wang  <https://orcid.org/0000-0002-6026-2139>

Kun Luo  <https://orcid.org/0000-0003-3644-9400>

REFERENCES

- Bates RB, Ghoniem AF, Jablonski WS, et al. Steam-air blown bubbling fluidized bed biomass gasification (BFBGG): multi-scale models and experimental validation. *AIChE J.* 2017;63(5):1543-1565.
- Ong Z, Cheng Y, Maneerung T, et al. Co-gasification of woody biomass and sewage sludge in a fixed-bed downdraft gasifier. *AIChE J.* 2015;61(8):2508-2521.
- Mettler MS, Vlachos DG, Dauenhauer PJ. Top ten fundamental challenges of biomass pyrolysis for biofuels. *Energ Environ Sci.* 2012;5(7):7797-7809.
- Bridgwater AV. Review of fast pyrolysis of biomass and product upgrading. *Biomass Bioenergy.* 2012;38:68-94.

5. Koppatz S, Pfeifer C, Rauch R, Hofbauer H, Marquard-Moellenstedt T, Specht M. H₂ rich product gas by steam gasification of biomass with in situ CO₂ absorption in a dual fluidized bed system of 8 MW fuel input. *Fuel Process Technol.* 2009;90(7):914-921.
6. Chen S, Wang D, Xue Z, Sun X, Xiang W. Calcium looping gasification for high-concentration hydrogen production with CO₂ capture in a novel compact fluidized bed: simulation and operation requirements. *Int J Hydrogen Energy.* 2011;36(8):4887-4899.
7. Han L, Wang Q, Yang Y, Yu C, Fang M, Luo Z. Hydrogen production via CaO sorption enhanced anaerobic gasification of sawdust in a bubbling fluidized bed. *Int J Hydrogen Energy.* 2011;36(8):4820-4829.
8. Balat M, Balat M, Kirtay E, Balat H. Main routes for the thermo-conversion of biomass into fuels and chemicals. Part 2: gasification systems. *Energ Conver Manage.* 2009;50(12):3158-3168.
9. Dudukovic MP. Frontiers in reactor engineering. *Science.* 2009;325(5941):698-701.
10. Gerber S, Behrendt F, Oevermann M. An Eulerian modeling approach of wood gasification in a bubbling fluidized bed reactor using char as bed material. *Fuel (Lond).* 2010;89(10):2903-2917.
11. Wang X, Jin B, Zhong W. Three-dimensional simulation of fluidized bed coal gasification. *Chem Eng Process Process Intensif.* 2009;48(2):695-705.
12. Tsuji Y, Kawaguchi T, Tanaka T. Discrete particle simulation of two-dimensional fluidized bed. *Powder Technol.* 1993;77(1):79-87.
13. Wang S, Luo K, Hu C, Sun L, Fan J. Impact of operating parameters on biomass gasification in a fluidized bed reactor: an Eulerian-Lagrangian approach. *Powder Technol.* 2018;333:304-316.
14. Yang M, Zhang J, Zhong S, et al. CFD modeling of biomass combustion and gasification in fluidized bed reactors using a distribution kernel method. *Combust Flame.* 2022;236:111744.
15. Kong D, Wang S, Luo K, Hu C, Li D, Fan J. Three-dimensional simulation of biomass gasification in a full-loop pilot-scale dual fluidized bed with complex geometric structure. *Renew Energy.* 2020;157:466-481.
16. Yang S, Wang S, Wang H. Numerical study of biomass gasification in a 0.3 MWth full-loop circulating fluidized bed gasifier. *Energ Conver Manage.* 2020;223:113439.
17. Kraft S, Kirnbauer F, Hofbauer H. CFPD simulations of an industrial-sized dual fluidized bed steam gasification system of biomass with 8 MW fuel input. *Appl Energy.* 2017;190:408-420.
18. Andrews MJ, O'Rourke PJ. The multiphase particle-in-cell (MP-PIC) method for dense particulate flows. *Int J Multiph Flow.* 1996;22(2):379-402.
19. Snider DM. An incompressible three-dimensional multiphase particle-in-cell model for dense particle flows. *J Comput Phys.* 2001;170(2):523-549.
20. Udomsirikakorn J, Basu P, Salam PA, Acharya B. Effect of CaO on tar reforming to hydrogen-enriched gas with in-process CO₂ capture in a bubbling fluidized bed biomass steam gasifier. *Int J Hydrogen Energy.* 2013;38(34):14495-14504.
21. Song T, Wu J, Shen L, Xiao J. Experimental investigation on hydrogen production from biomass gasification in interconnected fluidized beds. *Biomass Bioenergy.* 2012;36:258-267.
22. Kong D, Luo K, Wang S, Yu J, Fan J. Particle behaviours of biomass gasification in a bubbling fluidized bed. *Chem Eng J.* 2022;428:131847.
23. Loha C, Chattopadhyay H, Chatterjee PK. Three dimensional kinetic modeling of fluidized bed biomass gasification. *Chem Eng Sci.* 2014;109:53-64.
24. Liu H, Cattolica RJ, Seiser R, Liao C. Three-dimensional full-loop simulation of a dual fluidized-bed biomass gasifier. *Appl Energy.* 2015;160:489-501.
25. Jemaa M, Abbassi MA, Guedri K, et al. Kinetic and characteristic studies on the pyrolysis of vine stems, almond shell and Ziziphus wood using thermo-gravimetric analysis (TGA). 2016.
26. Prakash N, Karunanithi T. Kinetic modeling in biomass pyrolysis - a review. *Journal of Applied Sciences Research.* 2008;4(12):1627-1636.
27. Abani N, Ghoniem AF. Large eddy simulations of coal gasification in an entrained flow gasifier. *Fuel (Lond).* 2013;104:664-680.
28. Jones WP, Lindstedt RP. Global reaction schemes for hydrocarbon combustion. *Combust Flame.* 1988;73(3):233-249.
29. Gómez-Barea A, Leckner B. Modeling of biomass gasification in fluidized bed. *Prog Energy Combust Sci.* 2010;36(4):444-509.
30. Bustamante F, Enick RM, Killmeyer RP, et al. Uncatalyzed and wall-catalyzed forward water-gas shift reaction kinetics. *AIChE J.* 2005;51(5):1440-1454.
31. Baker EH. 87. The calcium oxide-carbon dioxide system in the pressure range 1-300 atmospheres. *J Chem Soc.* 1962;1:464-470.
32. Koppatz S, Pfeifer C, Rauch R, Hofbauer H, Marquard-Moellenstedt T, Specht M. H₂ rich product gas by steam gasification of biomass with in situ CO₂ absorption in a dual fluidized bed system of 8MW fuel input. *Fuel Process Technol.* 2009;90(7-8):914-921.
33. Sun P, Grace JR, Lim CJ, Anthony EJ. Determination of intrinsic rate constants of the CaO-CO₂ reaction. *Chem Eng Sci.* 2008;63(1):47-56.
34. Li T, Dietiker J, Zhang Y, Shahnam M. Cartesian grid simulations of bubbling fluidized beds with a horizontal tube bundle. *Chem Eng Sci.* 2011;66(23):6220-6231.
35. Lu L, Konan A, Benyahia S. Influence of grid resolution, parcel size and drag models on bubbling fluidized bed simulation. *Chem Eng J.* 2017;326:627-639.
36. Laverman JA, Roghair I, Annaland MVS, Kuipers H. Investigation into the hydrodynamics of gas-solid fluidized beds using particle image velocimetry coupled with digital image analysis. *Can J Chem Eng.* 2008;86(3):523-535.
37. Liu H, Li J, Wang Q. Simulation of gas-solid flow characteristics in a circulating fluidized bed based on a computational particle fluid dynamics model. *Powder Technol.* 2017;321:132-142.
38. Xie J, Zhong W, Shao Y, Liu Q, Liu L, Liu G. Simulation of combustion of municipal solid waste and coal in an industrial-scale circulating fluidized bed boiler. *Energy Fuel.* 2017;31(12):14248-14261.
39. Wang S, Luo K, Fan J. CFD-DEM coupled with thermochemical sub-models for biomass gasification: validation and sensitivity analysis. *Chem Eng Sci.* 2020;217:115550.
40. Li C, Eri Q. Comparison between two Eulerian-Lagrangian methods: CFD-DEM and MPPIC on the biomass gasification in a fluidized bed. *Biomass Convers Biorefin.* 2021;13:1-18.
41. Hwang IS, Sohn J, Do Lee U, Hwang J. CFD-DEM simulation of air-blown gasification of biomass in a bubbling fluidized bed gasifier: effects of equivalence ratio and fluidization number. *Energy (Oxf).* 2021;219:119533.

SUPPORTING INFORMATION

Additional supporting information can be found online in the Supporting Information section at the end of this article.

How to cite this article: Kong D, Wang S, Luo K, Fan J. Numerical study of biomass gasification combined with CO₂ absorption in a bubbling fluidized bed. *AIChE J.* 2023;69(8):e18096. doi:10.1002/aic.18096